nature communications

Article

https://doi.org/10.1038/s41467-025-63894-1

In situ secondary structure imaging of protein phase separation and aggregation by hyperspectral stimulated Raman scattering microscopy

Received: 12 June 2025

Accepted: 28 August 2025

Published online: 29 September 2025

Check for updates

Ruifeng Sun[1], Yanrong Zhuang[2], Yi Lin[2] ✉ & Fanghao Hu[1] ✉

Biomolecular condensates enable the coordination of cellular activities with high spatiotemporal selectivity. Many techniques have been developed to characterize protein condensate. However, direct visualization of protein structure in phase-separated condensate remains underexplored. Here we develop in situ quantitative imaging of secondary structure in protein condensates by stimulated Raman scattering (SRS) microscopy. Characteristic spectra of four secondary structures are obtained from protein amide I vibration analysis. Hyperspectral SRS imaging reveals significant enrichments and disordered to ordered structural changes during phase separation of ALS-related proteins. Time-lapse imaging of protein aging process directly visualizes heterogeneous β-sheet formation on the condensate surface. And secondary structures of mutant proteins are imaged to correlate amino acid sequence to phase separation property. Live-cell label-free imaging of protein structure is further demonstrated to exhibit pronounced heterogeneity in subcellular aggregates. Therefore, our technique provides crucial molecular-level information to investigate protein phase separation and its transition in pathological aggregation.

Proteins form certain folded structures from secondary, tertiary, to quaternary structures, the correct folding of which is essential to their physiological functions. Misfolded protein structure can lead to loss of function, cytotoxicity, and eventually cell death. Moreover, protein misfolding and abnormal aggregation have been found to be a hallmark in many neurodegenerative diseases, including Alzheimer's, Huntington's disease, and amyotrophic lateral sclerosis (ALS)[1]. To investigate protein structure and its transformation will facilitate the understanding of molecular mechanism in cellular activities and their dysregulation in diseases.

Recently, biomolecular condensates have been shown to play important roles in regulating protein function, which are formed reversibly with high fluidity and maintain dynamic exchange with the surrounding environment[2]. The formation of protein condensates has been proposed to be driven by liquid–liquid phase separation (LLPS), through multivalent interaction and/or protein low-complexity domain (LCD)[3–6]. Under genetic mutation or external stress, aberrant protein condensate might irreversibly convert from a liquid-like state to solid-like protein aggregates, which have been implicated in the disease development[7]. However, how protein transitions from physiological to pathological state at the molecular level remains poorly understood, largely due to limited technique to image protein structure under native environment.

To study protein structure in situ, many efforts have been carried out in recent years. Structural biology techniques, including X-ray diffraction (XRD)[8], cryo-electron microscopy (cryo-EM)[9], and nuclear

[1]Department of Chemistry, Ministry of Education Key Laboratory of Bioorganic Phosphorus Chemistry and Chemical Biology, Tsinghua University, Beijing, China. [2]State Key Laboratory of Membrane Biology, IDG/McGovern Institute for Brain Research, Tsinghua-Peking Joint Centre for Life Sciences, School of Life Sciences, Tsinghua University, Beijing, China. ✉e-mail: linyi@mail.tsinghua.edu.cn; hufanghao@tsinghua.edu.cn

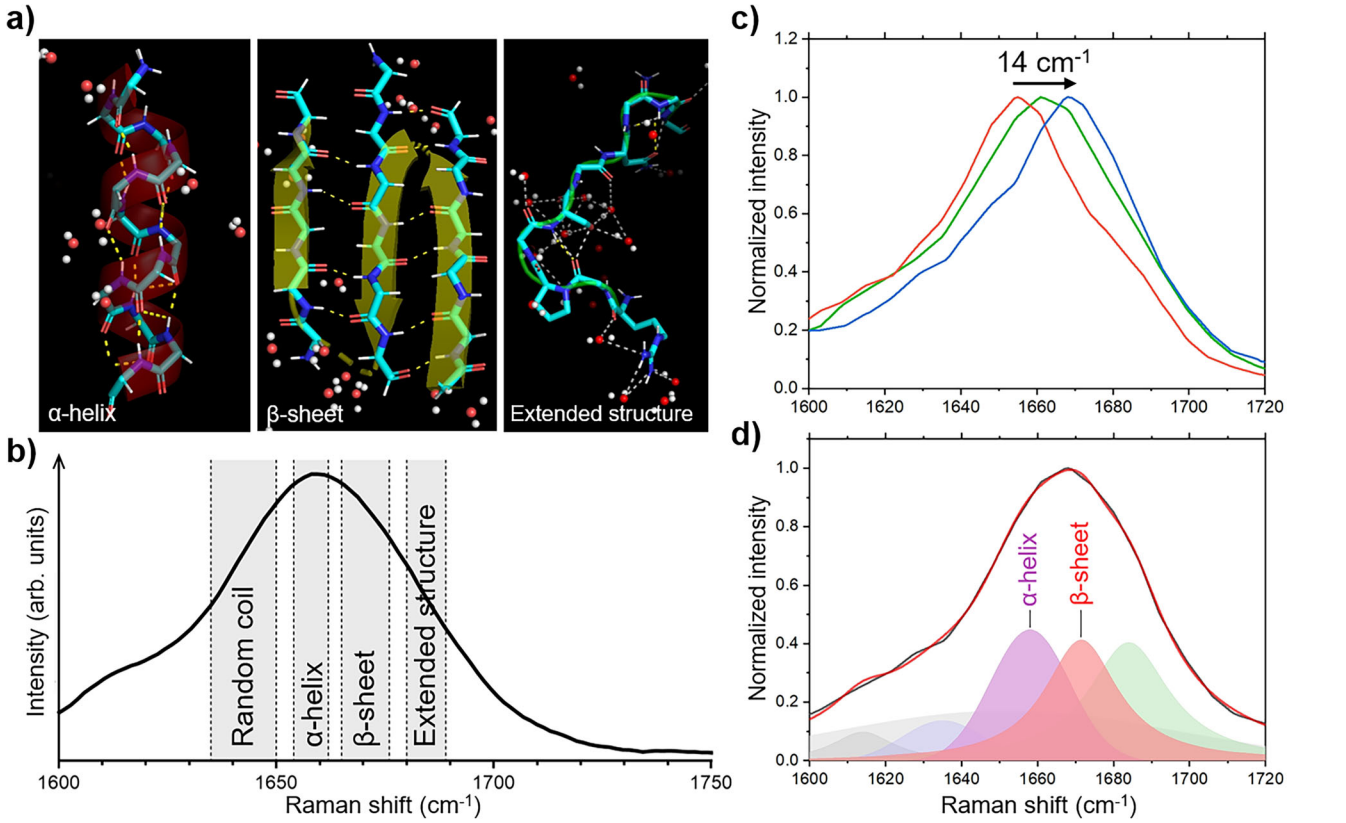

Fig. 1 | Protein secondary structure and Raman frequency in the amide I band. **a** Representative amide backbone of α-helix, β-sheet, and extended structure shown with carbon (cyan), nitrogen (blue), oxygen (red), and hydrogen (white). α-helix and β-sheet showed extensive hydrogen bonding within the backbone (yellow dashed line), while the extended structure showed increased hydrogen bonding with water (white dashed line). **b** Four secondary structures exhibited resolvable frequency regions (shaded areas) in the amide I Raman band. **c** SRS spectra of BSA (red), lysozyme (green), and lysozyme fibril (blue) displayed a 14 cm^{-1} peak shift in the amide I band. **d** Spectral fitting of protein amide I band with four secondary structures (colored areas). Source data are provided as a Source data file.

magnetic resonance (NMR) spectroscopy[10,11], are powerful and can provide full structures at the atomic level. But they often require special sample manipulation in an isolated system, and suffer from reduced contrast and sensitivity under native conditions, which are not ideal for investigating phase-separated condensates with heterogeneous structures and dynamics.

Optical techniques such as fluorescence microscopy can achieve in situ imaging of protein, but require fluorescent label with limited structural information. Vibrational spectroscopy, including infrared (IR) and Raman, is highly sensitive to molecular structure, and has been applied to study protein structure based on characteristic chemical bond vibrations such as the amide I band[12–16]. With rich information, analysis of protein secondary structure by spectral decomposition has been demonstrated in multiple systems by IR[17–20] and Raman spectroscopy[21–25], but is usually limited by weak signal or reduced resolution for in situ imaging.

Stimulated Raman scattering microscopy can increase vibrational transition rate by up to 10^8 folds through quantum amplification, and enhance the imaging speed by over 1000 times[26,27]. Based on intrinsic chemical bond vibrations, SRS microscopy has achieved label-free molecular imaging in many systems with high sensitivity and sub-micron resolution[28–36]. Compared to IR absorption-based techniques, SRS is fully compatible with aqueous biological conditions and achieves high imaging resolution. Unlike coherent anti-Stokes Raman scattering microscopy that requires Kramers–Kronig transform to compute Raman-like spectrum[11,37], SRS spectrum is free from spectral distortion and non-resonant background, which is advantageous for spectroscopic analysis with high fidelity.

Here, we develop a quantitative imaging technique to visualize protein secondary structure in situ by label-free hyperspectral SRS microscopy. Characteristic Raman spectra of four secondary structures are extracted from the protein amide I band, and quantitative SRS imaging of protein secondary structure is demonstrated with high sensitivity and accuracy. We apply the technique to image structural change and spatial heterogeneity during phase separation of a series of ALS-related proteins, which show significant enhancement of ordered structures in phase-separated protein condensates. In addition, time-lapse tracking of single condensate reveals that β-sheet-rich domains first appear on the surface to undergo liquid-to-solid phase transition during the aging of fused in sarcoma (FUS) protein. Furthermore, site-specific mutations in ataxin-2 (ATXN2) protein LCDs are shown to strongly modulate secondary structures along with phase separation properties. Lastly, label-free secondary structure imaging is demonstrated in live mammalian cells, exhibiting heterogeneous patterns of huntingtin aggregates. Together, quantitative hyperspectral SRS imaging of secondary structure offers a powerful tool with strong potential in elucidating protein structural transition during phase separation, protein aging processes, and pathogenic mutations.

Results

Characteristic Raman spectra of protein secondary structure in the amide I band

Protein secondary structure represents local spatial arrangement of polypeptide backbone (Fig. 1a), and amide I Raman band (1600–1700 cm^{-1}), mainly from backbone C=O stretching, is especially sensitive to protein secondary structure[21]. Depending on dihedral

angle, hydrogen bonding, and solvation environment, amide I band can be separated into four regions with resolvable Raman frequencies (Fig. 1b), including random coil (RC, 1635–1650 cm^{-1}), α-helix (1654–1662 cm^{-1}), β-sheet (1665–1676 cm^{-1}), and extended structure (1680–1689 cm^{-1})[16,21–23]. The extended structure includes polyproline II conformation, loose β-strand, and different turns[23,24], with increased solvent exposure and reduced protein interaction, compared to α-helix and β-sheet.

We performed spectral fitting of the amide I band on five proteins with distinct structures, including bovine serum albumin (BSA), ovalbumin (OVA), enhanced green fluorescent protein, lysozyme, and lysozyme fibril. For instance, BSA is rich in α-helix, OVA contains a comparable amount of α-helix and β-sheet, and lysozyme fibril exhibits high β-sheet content. SRS spectra of protein amide I band showed a significant peak shift of 14 cm^{-1} between BSA and lysozyme fibril (Fig. 1c), displaying high structural sensitivity.

Two Lorentzian and three Gaussian peaks (Supplementary Table 1), corresponding to four types of secondary structures and a water OH bending mode[38], were chosen based on best fit and chi-squared test, and applied to fit all protein spectra using a single set of frequency and linewidth parameter (Fig. 1d and Supplementary Fig. 1). Secondary structure percentages were calculated with relative peak intensities, considering amide I Raman cross section of each secondary structure is nearly identical[21]. Indeed, we showed that spectral fitting closely reflected protein secondary structure composition with <5% deviation from reported values (Supplementary Table 2), and demonstrated the correct assignment of secondary structure in the protein amide I band.

More importantly, we noticed that five different proteins exhibited highly consistent Raman spectra for each secondary structure (Supplementary Fig. 2). The average peak frequency and full width half maximum (FWHM) were: random coil at 1636.4 ± 2.3 cm^{-1} (30.5 ± 4.1 cm^{-1}), α-helix at 1657.5 ± 0.8 cm^{-1} (27.3 ± 4.7 cm^{-1}), β-sheet at 1671.2 ± 1.1 cm^{-1} (23.7 ± 4.4 cm^{-1}), and extended structure at 1685.0 ± 1.1 cm^{-1} (24.3 ± 4.6 cm^{-1}). Not only standard deviations of peak frequencies were within 2 cm^{-1}, but also those of FWHM in linewidth were within 5 cm^{-1}. We further performed correlative CD-SRS measurements on protein samples exhibiting mainly a single type of secondary structure, which confirmed the Raman peak assignments (Supplementary Fig. 3) and was supported by the second derivative of amide I spectra (Supplementary Fig. 4). This demonstrated that secondary structure as a fundamental building block of protein maintained a stable profile in the amide I Raman spectrum. We thus referred them as characteristic Raman spectra of four secondary structures.

Quantitative imaging of secondary structure by label-free hyperspectral SRS microscopy

With characteristic spectra of protein secondary structure, hyperspectral SRS imaging was performed at five well-resolved frequencies, including 1638 cm^{-1}, 1657 cm^{-1}, 1672 cm^{-1}, 1689 cm^{-1}, and 1730 cm^{-1} (Fig. 2a). Quantitative images of four secondary structures and water distribution were obtained by linear unmixing with a five-by-five matrix ($P_{5\times5}$) (Fig. 2b and Supplementary Note 1). Secondary structure percentage was calculated through dividing average intensity in each image by their sum.

We validated hyperspectral SRS imaging of secondary structure on proteins chosen above (Fig. 2c and Supplementary Fig. 5), which again showed quantitative values with high consistency (Fig. 2d and Supplementary Table 3). For example, structural imaging of BSA showed 64% α-helix and little β-sheet, and OVA exhibited 32% α-helix and 27% β-sheet. Moreover, lysozyme showed a drastic increase of β-sheets by 60% and a reduction in α-helices upon aggregation, which was clearly shown by in situ imaging of lysozyme fibril (Fig. 2c). This demonstrated that our method can visualize not only a large range of secondary structure composition, but more importantly, quantitative change during structural transformation.

In addition, we imaged five proteins not applied in spectral fitting, including human serum albumin, trypsin, β-lactoglobulin, papain, and phosvitin (Supplementary Fig. 6), which also show consistent results with reported values (Supplementary Table 3). The uncertainty of secondary structure imaging was further estimated to be <5%, when the signal to noise ratio (S/N) of SRS images were larger than 30 (Supplementary Fig. 7). Indeed, all structural imaging was repeated for more than five times with high sensitivity (Supplementary Figs. 5, 6), and standard deviations were within 7% for most proteins (Supplementary Table 3). Therefore, we have successfully obtained characteristic Raman spectra of four secondary structures and demonstrated label-free quantitative structural imaging of various proteins with high accuracy.

In situ secondary structure imaging of protein phase separation

Protein phase separation has drawn increasing attention with its dynamic nature and diverse cellular function, and intrinsically disordered LCDs are suggested to mediate the formation of protein condensates[4,5]. Moreover, protein enrichment in phase-separated condensate is beneficial to hyperspectral SRS imaging with enhanced sensitivity. We thus applied in situ quantitative imaging to visualize protein composition and secondary structure during in vitro phase separation of ALS-related FUS and ATXN2 LCDs (Fig. 3).

Under a bright-field microscope, both FUS LCD (residues 1-214) and ATXN2 LCD (residues 1125-1312) formed clear condensates after dilution from guanidine buffer to neutral Tris-HCl buffer (Supplementary Fig. 8). The guanidine buffer effectively maintained a well-mixed protein solution, preventing phase separation and thus being termed the dispersed state. Phase-separated protein condensates spontaneously formed in the Tris-HCl buffer, which was termed the condensed state. Fluorescence recovery after photobleaching (FRAP) experiments demonstrated rapid intensity recovery in both protein condensates (Supplementary Fig. 8), indicating a liquid-like phase characterized by high fluidity.

We first quantified protein concentration in both condensates (Fig. 3a, b). Protein CH_3 vibration has been shown to be suitable for independent concentration measurement[33]. To exclude the effect of different protein sequences and structures, BSA were measured in both Tris-HCl and guanidine buffers to exhibit nearly identical calibration curves to that of ATXN2 (Supplementary Fig. 9). SRS imaging of protein CH_3 showed uniform distribution across condensates, with average concentrations of 19.5 mM for FUS LCD and 21.4 mM for ATXN2 LCD (Fig. 3b). Protein concentration in the surrounding dilute solution was measured to be 100–120 μM by UV-Vis absorption (Supplementary Fig. 10), corresponding to over 150-fold enrichments in both condensates[39].

We next performed in situ secondary structure imaging of dispersed and condensed protein states, which exhibited significant changes after phase separation (Fig. 3c). With concentration enrichment, hyperspectral SRS images of amide I band can readily achieve S/N > 35 for structural imaging with high accuracy (Supplementary Fig. 11). Interestingly, in the unmixed images of condensed states, we first noticed holes in the water channel with reduced intensity, which was quantified to be ~70% of the dilute solution outside (Supplementary Fig. 12). This indicated the release of water from condensates after phase separation[40–42], which was likely to influence protein structure through reduced hydration with a less dynamic hydrogen-bonded network[20,43,44].

Indeed, quantitative secondary structure results revealed a large conversion from disordered structure to β-sheet in both condensates (Fig. 3d). In the dispersed state, FUS LCD (51%) and ATXN2 LCD (48%) exhibited mainly extended structures, indicating a well-solvated conformation with high structural flexibility. After phase separation,

https://doi.org/10.1038/s41467-025-63894-1

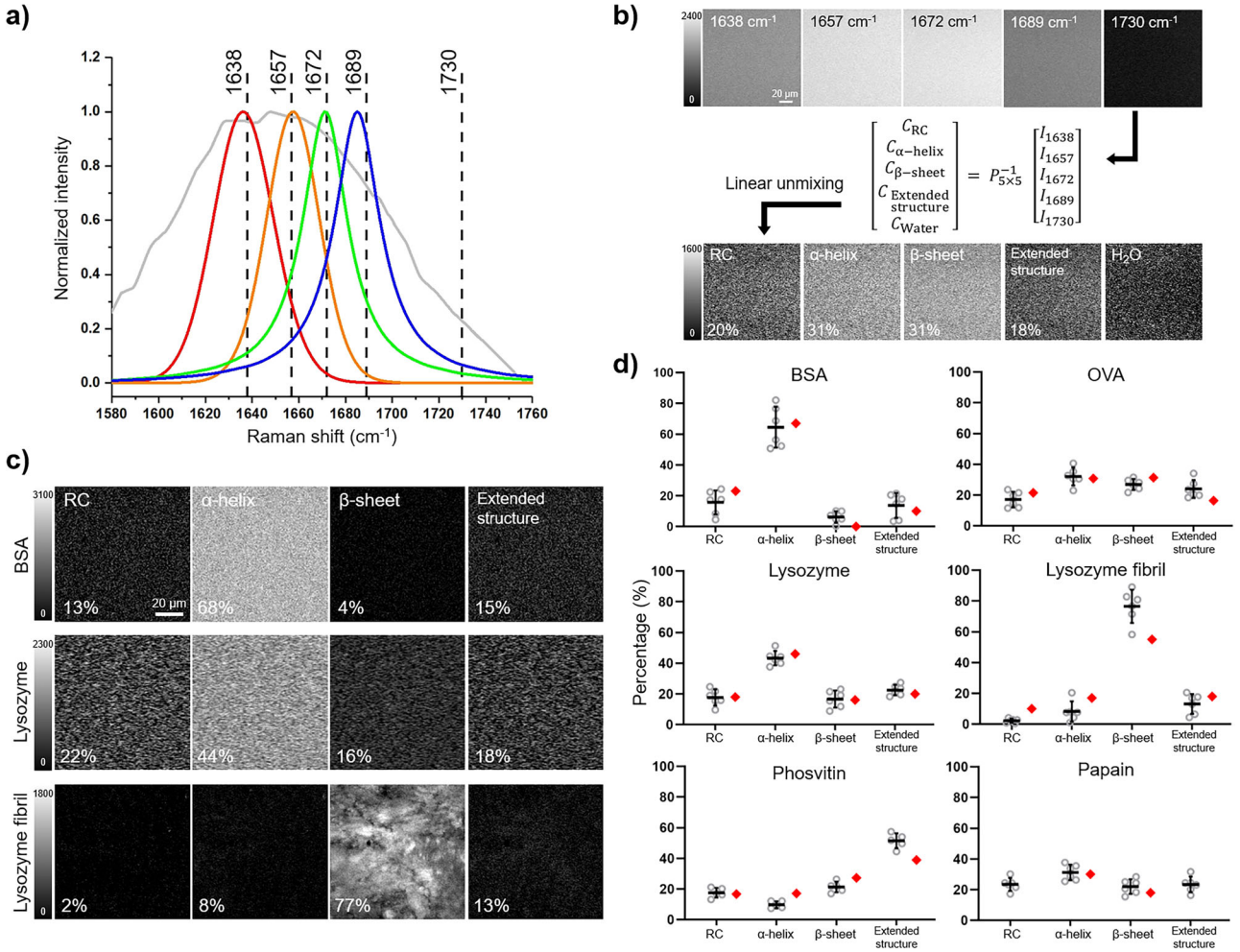

Fig. 2 | Quantitative imaging of protein secondary structure by hyperspectral SRS microscopy. a Characteristic Raman spectra of four secondary structures, including random coil (red), α-helix (orange), β-sheet (green), and extended structure (blue). Water OH bending spectrum measured experimentally (gray) was shown in the background, and five SRS imaging wavenumbers were indicated. **b** Quantitative secondary structure imaging by hyperspectral SRS coupled with linear unmixing. After subtracting the off-resonance image, SRS images at five wavenumbers were multiplied with the inverse of coefficient matrix $P_{5\times5}$ to obtain quantitative images of secondary structure and water. $P_{5\times5}$ matrix was obtained from normalized Raman spectra of four secondary structures and water. **c** Representative secondary structure images of BSA, lysozyme solution, and lysozyme fibril with distinct structural compositions. Percentage values were shown for a single experiment. **d** Protein secondary structure quantification by hyperspectral SRS imaging (black) and reported values (red). All experiments were repeated independently with similar results and the data were shown as mean ± s.d. (BSA, OVA, lysozyme, lysozyme fibril, papain, $n = 6$; phosvitin, $n = 5$ independent experiments). Source data are provided as a Source data file.

extended structures decreased strongly from 51% to 36%, and β-sheets increased from 13% to 24% for FUS LCD. Similarly, significant conversion of extended structures to β-sheets was observed in ATXN2 LCD condensates. Meanwhile, α-helix exhibited small changes for both proteins. This demonstrated that substantial structural change occurred in protein LCDs during phase separation. Together with decreased water in protein condensates, it may suggest a driving force in LLPS by reducing water solvation and enhancing protein self-interaction via increased entropy of released water[45,46] and disordered to ordered structural transition[20,47].

Thus, by in situ hyperspectral SRS imaging, we have provided quantitative protein concentration, water content, and secondary structure change in phase-separated condensates with rich information.

Time-lapse structural imaging of FUS LCD condensates during aging process

Aging of protein condensate can lead to the formation of irreversible aggregates or amyloids, which have been implicated in the development of neurodegenerative diseases[48,49]. ALS-associated FUS protein has been applied to investigate the aging process, where the fluidic protein condensates gradually convert to solid-like aggregates through liquid-to-solid phase transition. To gain deeper insights, we performed time-lapse secondary structure imaging of phase-separated FUS LCDs to visualize structural transformation and spatial heterogeneity during the protein aging process (Fig. 4).

FUS LCD condensates were incubated in a neutral Tris-HCl buffer containing dextran. During the aging process, a transition from liquid to solid phase was observed (Supplementary Fig. 13). At the initial time point of 0 h, protein condensates exhibited a circular shape, which was attributed to the reduced surface tension characteristic of the liquid-like phase. After aging for 8 h, there was a noticeable increase in β-sheets, as shown in Fig. 4a and Supplementary Fig. 14. Through overlaying the β-sheet and extended structure images captured over time, clear structural heterogeneity was revealed on a single condensate (Fig. 4b). The circular region maintained a similar composition of β-sheets as observed at 0 h, while the irregular region showed a significantly increase in β-sheets to 27%,

https://doi.org/10.1038/s41467-025-63894-1

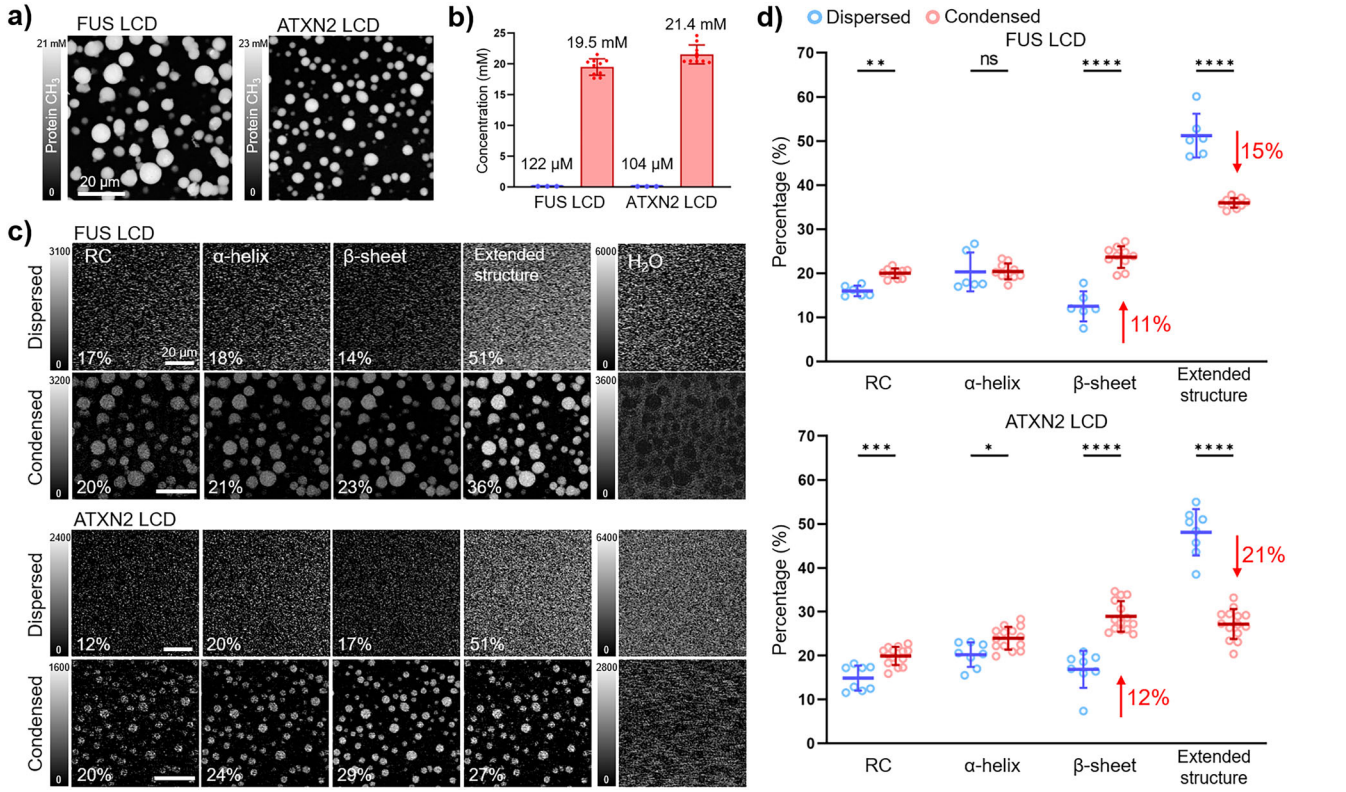

Fig. 3 | In situ SRS imaging of FUS and ATXN2 LCD phase separation. a Protein CH_3 (2940 cm^{-1}) images of phase-separated condensates. **b** Concentration enrichments between the surrounding dilute solution (blue, $n = 3$ independent experiments) and the condensed state (red, $n = 10$ independent experiments) of both proteins. **c** Quantitative secondary structure images of FUS and ATXN2 LCDs in both dispersed and condensed states. Percentage values were shown for a single experiment. Water images were shown with reduced signal inside condensates. **d** Secondary structure quantification showed significant structural change between the dispersed (blue, FUS LCD, $n = 6$; ATXN2 LCD, $n = 8$ independent experiments) and condensed (red, FUS LCD, $n = 10$; ATXN2 LCD, $n = 14$ independent experiments) states of both proteins. All data were shown as mean ± s.d. Two-tailed *t*-test was used, $^{*}p < 0.05$, $^{**}p < 0.01$, $^{***}p < 0.001$, $^{****}p < 0.0001$. Source data are provided as a Source data file.

indicating the formation of a locally ordered structure with enhanced rigidity. FRAP analysis further supported the co-existence of liquid-like and solid-like phases on single condensates, with distinct recovery level and fluidity observed at both 8 and 14 h of aging (Supplementary Fig. 13).

After 48 h, most FUS LCD condensates were transformed into irregular β-sheet-dominant (35%) structures with a drastically reduced FRAP rate (Fig. 4b). Overall, β-sheets increased significantly by 10% and extended structures decreased by 9% from liquid-like condensates to solid-like aggregates (Fig. 4c). Meanwhile, protein concentration increased from 19.9 mM in condensates at 0 h to 26.2 mM in aggregates at 48 h (Fig. 4d), supporting molecular aggregation with densely-packed structures. Thioflavin T (ThT) staining exhibited enhanced fluorescence signal with time, suggesting amyloid formation (Supplementary Fig. 15).

Furthermore, time-lapse tracking of a single protein condensate verified significant structural conversion on the same droplet with spatially distinct regions (Supplementary Fig. 16). By closer examination during the first 8 h (Fig. 4e and Supplementary Movie 1), we observed the appearance of bright puncta first on the surface of protein condensates, which expanded in size with time and exhibited strong β-sheet contents. We also tracked the aging process of a disease-causing mutant G156E of FUS LCD[48], which showed a faster formation of β-sheets on condensates (Supplementary Fig. 17 and Supplementary Movie 2) and was consistent with its increased tendency in aggregation. Although a small domain at early time, β-sheet-rich region on the surface was likely to be the initiating site for liquid-to-solid phase transition during the aging of FUS protein, which might be explained by heterogeneous nucleation mechanism with enhanced intermolecular interaction in amyloid formation[50,51].

The accumulation of β-sheets could eventually result in the formation of cross-β structure in FUS fibrils[10]. Through in situ time-lapse secondary structure imaging, we directly visualized continual conversion to β-sheets and interfacial heterogeneity during the aging of FUS LCD condensates, where small β-sheet-rich domains initiated on the surface of protein condensate to gradually transition into solid-like aggregates. This showcased that our technique revealed not only quantitative structural change, but also spatial heterogeneity on single phase-separated condensate with high resolution, which was often lost in single-point or ensemble measurement.

Structural imaging of ATXN2 LCD condensates with amino acid mutation

Besides protein aging, amino acid sequence of LCDs has been shown to govern protein phase separation through various electrostatic and hydrophobic interactions[6,52]. With different side chains, proline and glutamine could tune physiological phase separation towards pathological aggregation, which have been found in neurological disease-related mutations[53]. To investigate the structural effect of amino acid mutation, we carried out in situ secondary structure imaging of mutant ATXN2 LCDs with site-specific glutamine to proline (Q-P) and proline to glutamine (P-Q) substitutions (Fig. 5 and Supplementary Fig. 18).

In a 4Q-P (Q1211, 1214, 1221, 1222 P) mutant, liquid-like protein condensates formed spontaneously with average concentration of 24.0 mM (Fig. 5a, b), and FRAP exhibited an increased intensity recovery than that of wild type (Fig. 5c). Compared to wild type structure,

https://doi.org/10.1038/s41467-025-63894-1

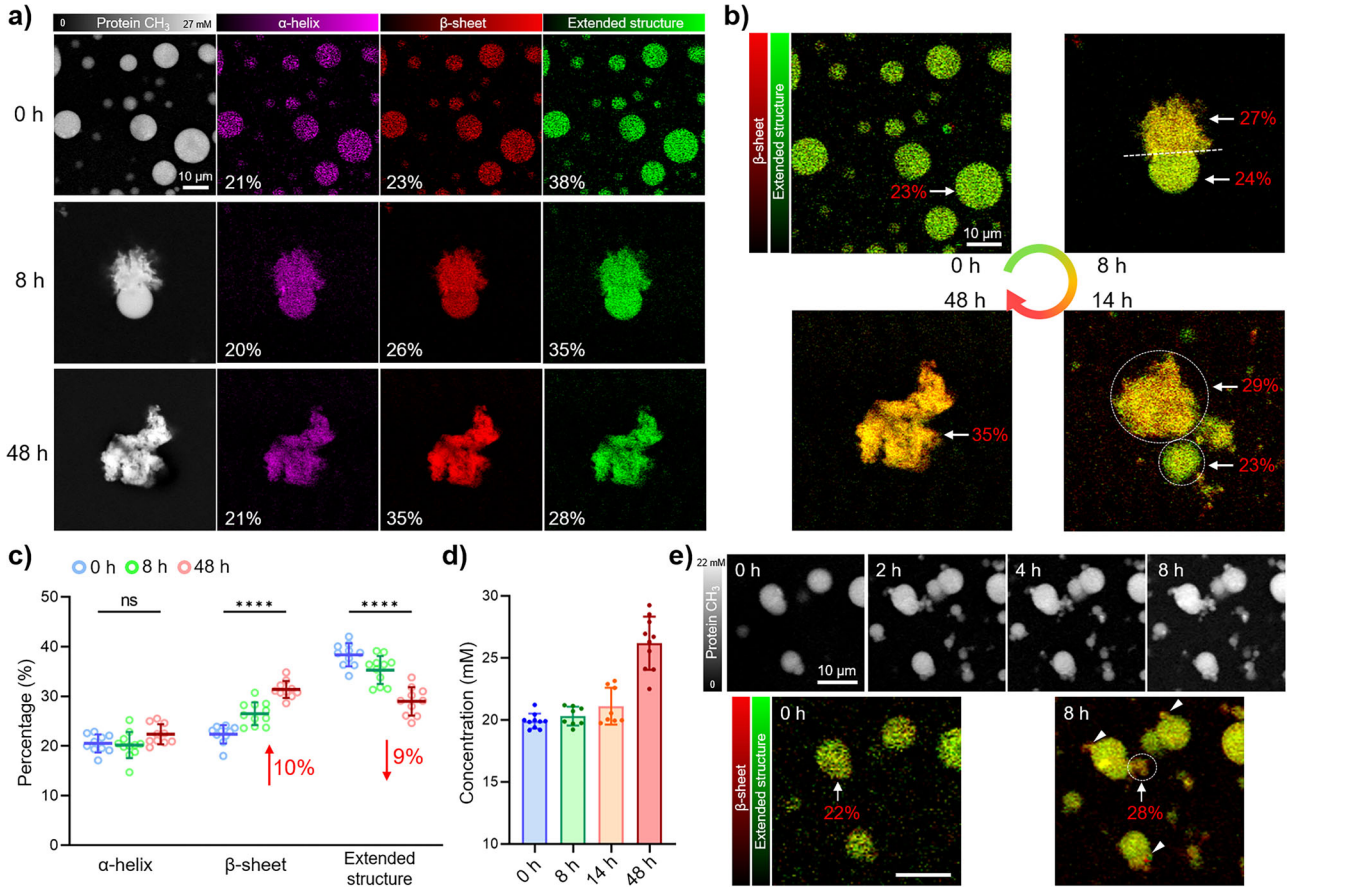

Fig. 4 | Time-lapse structural imaging of FUS LCD aging. a Protein CH_3 and secondary structure images of FUS LCD condensates at 0, 8, and 48 h of aging. Percentage values were shown for a single experiment. **b** Overlay images of β-sheet (red) and extended structure (green) in protein condensates at different time. Spatial heterogeneity of secondary structure was visualized on single condensates. β-sheet percentages (red) were shown for selected regions (white arrows). **c** Secondary structure quantification of FUS LCD condensates during aging showed continual increase of β-sheets (0 and 48 h, $n = 10$; 8 h, $n = 11$ independent experiments). **d** Protein concentration during aging of FUS LCD condensates (0 and 48 h, $n = 10$; 8 h and 14 h, $n = 8$ independent experiments). All data were shown as mean ± s.d. Two-tailed t-test was used. **e** Time-lapse single-condensate tracking showed heterogeneous β-sheet-rich puncta (arrowheads) appearing on the surface in overlay images. β-sheet percentages (red) were shown for selected regions (white arrows). Source data are provided as a Source data file.

secondary structure imaging revealed a 10% reduction of β-sheets and a drastically 12% increase of extended structures in the 4Q-P mutant (Fig. 5d). This indicated reduced protein interaction in 4Q-P LCDs, which exhibited increased molecular mobility and condensate fluidity.

On the contrary, for a 3P-Q (P1239, 1240, 1246Q) mutant, we observed the formation of protein aggregates, which is very different from liquid-like condensates for wild type and 4Q-P LCDs (Fig. 5a). Also, 3P-Q mutant exhibited a decreased protein concentration and much reduced recovery rate by FRAP (Fig. 5b, c), suggesting amorphous solid-like deposits. Moreover, secondary structure imaging showed a significant increase of β-sheets to 34% in 3P-Q mutant (Fig. 5d), suggesting enhanced ordered structure with low fluidity.

The opposite structural changes observed in mutant ATXN2 LCDs can be explained from two perspectives. First, proline, as a nonpolar amino acid with a cyclic side-chain, usually induces a bend in the protein backbone and disrupts long-range order. Second, polar glutamine favors both main-chain and side-chain hydrogen bonding, and enhances inter-strand association in β-sheets. Together, the 4Q-P mutant promoted disordered structure and condensate fluidity with weakened self-interaction, while the 3P-Q mutant increased intra/inter-protein hydrogen bonding to strengthen rigid β-sheets and drive liquid-like condensates towards hardened solid-like aggregates.

To examine further, we imaged three additional 2P-Q (P1239, 1240Q; P1239, 1246Q; P1240, 1246Q) mutant LCDs, which surprisingly showed similar condensate concentration and liquid-like fluidity as wild type (Fig. 5b, c and Supplementary Fig. 19). Consistently, all three mutants exhibited little change in secondary structure (Supplementary Fig. 20). This indicated that not all P-Q mutants led to structural change in phase-separated condensates, which was highly sensitive to the number of mutations. Single substitution of proline to glutamine near the threshold could tip the balance to cause significant perturbation in both protein structure and phase separation property, as shown by the 3P-Q mutant. Thus, we have visualized secondary structure changes related to specific amino acid mutations, facilitating our understanding of how protein sequences regulate phase separation at the molecular level.

Label-free secondary structure imaging of intracellular proteins

Investigating protein structure in cells is important to understand protein function in complex biological systems. Cellular species such as lipids and nucleic acids may interfere with secondary structure imaging due to overlapping frequencies, which can be largely circumvented by image segmentation to exclude nucleus and lipid-rich regions (Supplementary Fig. 21 and Supplementary Note 2) as verified in cells experimentally (Supplementary Fig. 22). Huntingtin (Htt) protein with polyglutamine expansion is a hallmark in Huntington's disease[54], and has been widely applied to study protein aggregation in cells. We carried out structural imaging of EGFP-labeled Htt exon 1 with a Q74 polyglutamine tract (EGFP-Htt-Q74) in live U-2 OS cells (Fig. 6a). Fluorescence imaging showed EGFP-Htt-Q74 formed large cytoplasmic

https://doi.org/10.1038/s41467-025-63894-1

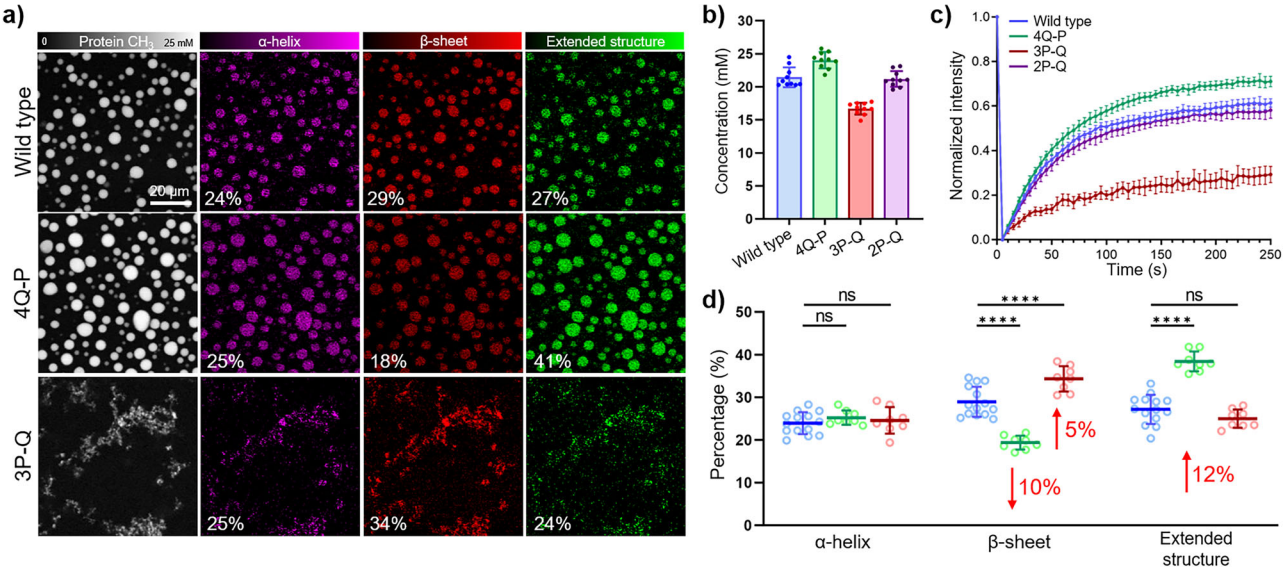

Fig. 5 | In situ secondary structure imaging of mutant ATXN2 LCDs. a Protein CH_3 and secondary structure images of wild type, 4Q-P (Q1211, 1214, 1221, 1222 P) mutant, and 3P-Q (P1239, 1240, 1246Q) mutant condensates. Percentage values were shown for a single experiment. **b** Protein concentrations of wild type, 4Q-P mutant, 3P-Q mutant, and 2P-Q (P1240, 1246Q) mutant condensates ($n = 10$ independent experiments for each condition). **c** FRAP curves in wild type and mutant condensates (wild type and 3P-Q, $n = 7$; 4Q-P, $n = 10$; 2P-Q, $n = 6$ independent experiments). **d** Secondary structure quantification of wild type (blue, $n = 14$), 4Q-P mutant (green, $n = 8$), and 3P-Q mutant (red, $n = 8$ independent experiments) condensates. All data were shown as mean ± s.d. Two-tailed t-test was used. Source data are provided as a Source data file.

inclusions, which were also visualized by SRS imaging of total proteins. In the total lipid channel, scattered signal was found to surround aggregates but with little intensity inside, indicating protein-dominated structure with negligible lipids. Secondary structure imaging of Htt aggregates showed strongly enhanced β-sheet contents (over 40%) (Fig. 6b and Supplementary Fig. 23), which doubled that of cytosolic proteins with an average 21% β-sheet in native cells (Supplementary Fig. 21).

Previous studies have indicated that EGFP labeling caused significant perturbations on Htt interaction[55,56], and β-barrel in EGFP affected secondary structure quantification. After removing EGFP, we can still visualize unlabeled Htt-Q74 aggregates in live cells by SRS imaging (Fig. 6c), which were confirmed by anti-Htt immunofluorescence with high specificity (Supplementary Fig. 24). Evident differences were first observed in the cytoplasmic Htt-Q74 aggregate, which exhibited a lipid ring in the outer region, indicating infiltration of membranous organelles[55]. Moreover, while total proteins appeared uniform, protein secondary structure imaging revealed a distinct core/shell morphology, which remained in cells after removing the lipids (Fig. 6c and Supplementary Fig. 25). We note that residual lipids can result in a higher α-helix content. Still, the core region exhibited reduced α-helices and increased β-sheets compared to the outer shell, suggesting possible aggregation through α-helix to β-sheet conversion from the center.

Furthermore, we observed two other types of unlabeled Htt-Q74 aggregates in live U-2 OS cells, including cytoplasmic aggregates without a lipid ring and nuclear aggregates. Both of these aggregates showed little lipids inside and no core-shell morphology, and there were significant increases in α-helix instead of β-sheet (Fig. 6d and Supplementary Fig. 26). We also imaged two types of cytoplasmic aggregates with distinct morphology and secondary structure in the same field of view (Supplementary Fig. 27). Further, the amide I SRS spectra of three types of unlabeled Htt-Q74 aggregates were measured in live cells to demonstrate clear spectral changes compared to cytosolic proteins and exhibit consistent results with hyperspectral structural imaging (Supplementary Figs. 28–30).

More quantitative differences can be evaluated between EGFP-Htt-Q74 and unlabeled Htt-Q74 aggregates. First, large structural heterogeneities were found for Htt-Q74 aggregates after removing EGFP label. Unlike EGFP-Htt-Q74 aggregates with 44% β-sheet, cytoplasmic Htt-Q74 aggregates with lipid ring showed a lowered β-sheet content to 38% (Fig. 6e), likely due to the removal of EGFP. For cytoplasmic and nuclear aggregates without a lipid ring, there was a further reduction in β-sheet to ~20% and strong increase in α-helix to ~50%, which might be associated with the helical N-terminus in oligomeric Htt aggregates with liquid-like state at the early stage[57,58]. Second, total mass concentration in unlabeled Htt-Q74 aggregates was measured to be 530–560 mg/mL (Fig. 6f), which was nearly 1.3-fold higher than that of EGFP-Htt-Q74 (434 mg/mL). Considering the large size of EGFP, protein molar concentration is expected to be even more different[56]. Through hyperspectral secondary structure imaging, we showed that EGFP label strongly perturbed Htt-Q74 aggregation and unlabeled Htt-Q74 formed three types of densely-packed aggregates, which exhibited distinct protein structure and distribution in live cells, highlighting the advantage of label-free structural imaging methods.

To further demonstrate the applicability, we employed this method to assess endogenous proteins in mouse tissues. Protein misfolding is prone to enhance in aging animals due to the loss of proteostasis, a phenomenon associated with the onset of age-related diseases[59]. In the liver tissues of 2-year-old mouse, SRS imaging identified stronger signal in the β-sheet channel, and ratio image of β-sheet over extended structure visualized a structural hotspot with ~8% increase in β-sheets compared to surrounding tissues (Supplementary Fig. 31), which was supported by measuring the amide I SRS spectra (Supplementary Fig. 32). Immuno-staining showed a strong co-localized signal of ataxin-2-like protein (Supplementary Fig. 31), suggesting misfolded proteins associated with stress granules[60]. Thus, label-free protein secondary structure imaging has been demonstrated in live cells and mouse tissues, which revealed quantitative structural change and heterogeneity in complex biological system.

https://doi.org/10.1038/s41467-025-63894-1

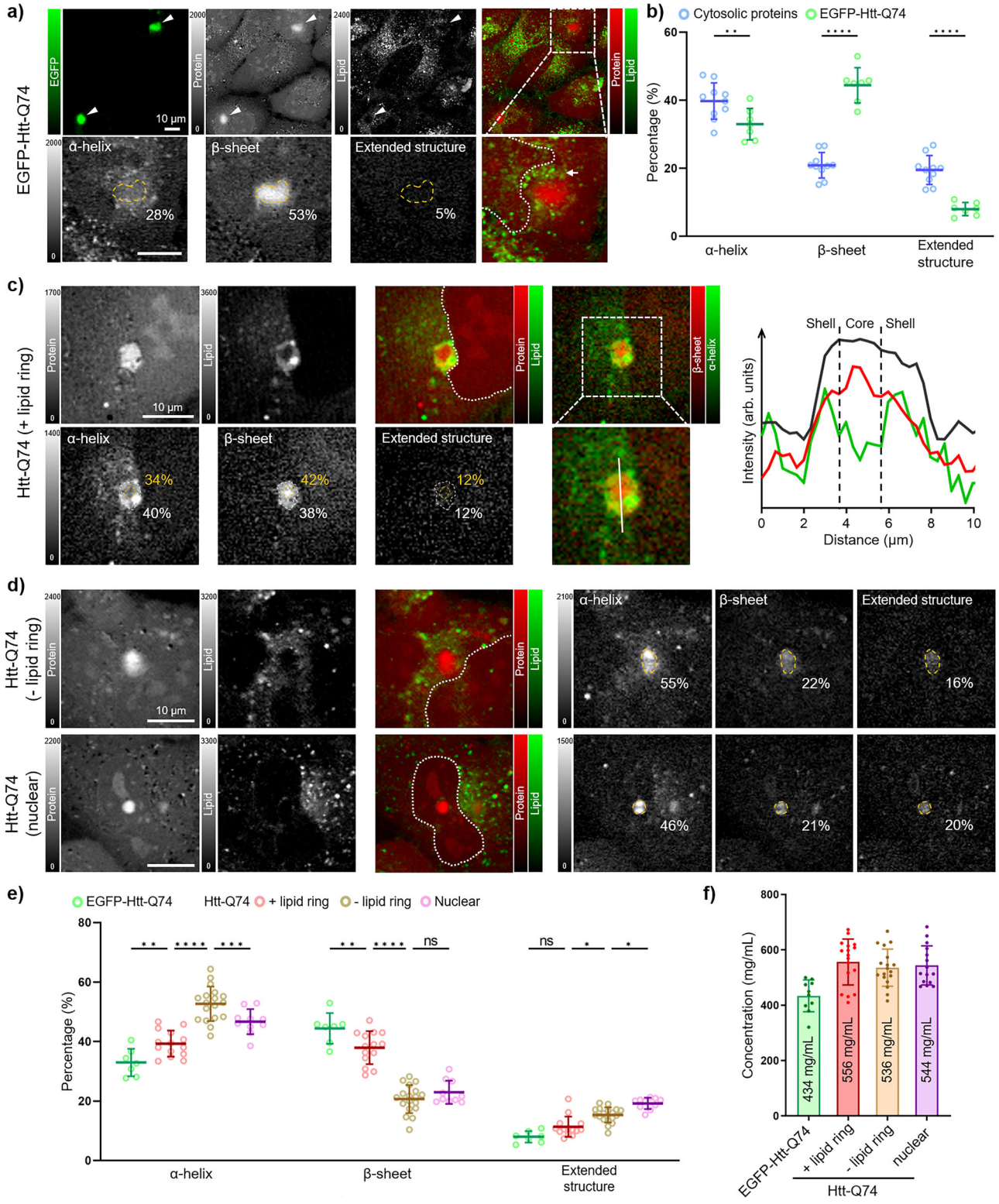

Discussion

Recent studies have highlighted the important relationship between protein structure and phase separation[53,61]. In this work, we have established a general method to quantitatively image protein secondary structure in situ through hyperspectral SRS of amide I vibration. In phase-separated condensates, we visualized a > 100-fold protein enrichment with water reduction and significant structural transformation from extended structures to β-sheets. Both reduced water content and disorder-to-order conversion could be synergetic in driving protein phase separation by balancing water solvation and intra/inter-protein interaction in favor of both enthalpy and entropy[45,46].

In addition, we have shown several key findings in protein phase separation. During the aging of FUS LCD, heterogeneous growth of β-sheet-rich regions was first visualized on the condensate surface to undergo liquid-to-solid phase transition through time-lapse structural tracking. Recently, surface aggregates were reported to promote liquid-to-solid transition during the maturation of FUS protein[62–64].

Fig. 6 | Label-free secondary structure imaging of Htt protein aggregates in live cells. a Fluorescence and SRS images of EGFP-Htt-Q74 aggregates in live U-2 OS cells. White arrowheads indicated two aggregates. In the magnified overlay image, nucleus (white dotted line) and lipids near the aggregate (white arrow) were indicated. Secondary structure percentages in aggregate were shown for selected region (yellow dashed circle). **b** Secondary structure quantification of cytosolic proteins (blue, $n = 10$) and EGFP-Htt-Q74 aggregates (green, $n = 7$ independent experiments). **c** Label-free SRS images of Htt-Q74 aggregates without EGFP. Protein aggregate with lipid ring was visualized near cell nucleus in the overlay image. Secondary structure percentages were shown for the core (yellow) and total (white) regions of selected aggregate (dashed circles). The line profile in Htt-Q74 aggregate indicated the spatial distribution of total proteins (black), α-helix (green), and β-sheet (red). **d** Label-free SRS images of two other types of Htt-Q74 aggregates, including cytoplasmic aggregates without lipid ring and nuclear aggregates. Secondary structure percentages were shown for selected aggregates (yellow dashed circles). **e** Secondary structure quantification of EGFP-Htt-Q74 aggregates (green, $n = 7$), Htt-Q74 aggregates with lipid ring (red, $n = 14$), without lipid ring (brown, $n = 18$), and nuclear aggregates (purple, $n = 10$ independent experiments). **f** Total protein concentrations of Htt-Q74 aggregates with and without EGFP (EGFP-Htt-Q74, $n = 10$; Htt-Q74 with lipid ring, $n = 18$; without lipid ring, $n = 17$; nuclear, $n = 15$ independent experiments). All data were shown as mean ± s.d. Two-tailed t-test was used. Source data are provided as a Source data file.

Compared to these studies, our technique didn't require fluorescent labeling or complicated spectral analysis, and provided direct visualization of interfacial secondary structure heterogeneity in situ.

Moreover, we related specific amino acid mutation to protein LCD structure in modulating phase separation, where proline promoted extended structures with reduced self-interaction in liquid-like condensates with high fluidity, and glutamine enhanced intra/inter-protein hydrogen bonding and ordered β-sheets to form hardened solid-like aggregates. This is consistent with a recent study that disease-related proline replacement can drive physiological LLPS towards pathological aggregation, by strengthening labile structure via main-chain hydrogen bonding in protein LCDs[53].

Furthermore, live-cell secondary structure imaging has been demonstrated to reveal protein aggregation heterogeneity with minimal perturbation. Three types of unlabeled Htt-Q74 aggregates were found with distinct secondary structures, suggesting different stages of Htt aggregation in live mammalian cells[55,57]. Helix-rich oligomeric aggregates may initially form and transition with time into sheet-rich structures from the core of the aggregates, which were sequestered by lipid interactions in the outer region. This showed high potential as a label-free approach to visualize protein misfolding in a complex system[33].

In situ structural imaging of phase-separated condensates by hyperspectral SRS has provided an important tool in studying protein state between homogeneous solution and solid aggregate, which is challenging for existing techniques. Conventional spectroscopy, such as solution NMR, lacks sufficient imaging capability and is difficult to characterize phase-separated proteins with slowed motion, broadened linewidth, and diminished signal[65]. Our method has filled a crucial gap to image phase-separated protein structure under native condition, which can be further improved. Label-free super-resolution SRS microscopy can be applied to visualize nanoscale structural heterogeneity[66]. And cryo-electron tomography[67] can be coupled for targeted characterization after in situ imaging.

To summarize, by investigating the composition and structural changes in protein condensates, we can gain molecular insights on the mechanism of phase separation and the pathogenesis of associated neurodegenerative diseases. In situ secondary structure imaging by SRS microscopy will find wide applications in studying structural transition and spatial heterogeneity of various proteins during LLPS-related processes.

Methods

Ethical statement

All animal experiments were conducted following the guidelines and approval of the Institutional Animal Care & Use Committee and the Animal Welfare and Ethics Committee of Tsinghua University under protocol number 19-LY1.

Stimulated Raman scattering (SRS) microscopy

An integrated laser system (picoEmerald, Applied Physics and Electronics, Inc.) produced synchronized pump and Stokes laser beams at 80 MHz repetition rate. The Stokes laser (1032.0 nm, 2 ps pulse width, 0.7 nm beam bandwidth) was intensity modulated by an electro-optic modulator at 10 MHz with >90% modulation depth, and the pump laser (tunable from 700 to 990 nm, 2 ps pulse width, 0.7 nm beam bandwidth) was generated by a built-in optical parametric oscillator. The laser beams were spatially and temporally overlapped using two dichroic mirrors and an integrated delay stage, and coupled into an inverted laser scanning microscope (Olympus, FV3000). Both laser beams were focused onto the sample through a 25× water objective (Olympus, XLPLN25XWMP, 1.05 N.A.). The transmitted beams were effectively collected by a high N.A. condenser lens (Olympus, oil immersion, 1.4 N.A.), and the Stokes beam was removed by a bandpass filter (CHROMA, ET890/220 m). The remaining pump beam was detected by a large area (10×10 mm^2) silicon photodiode (THORLABS, FDS1010) reversed biased at 64 DC voltage to increase the saturation threshold and reduce response time. The output current was terminated by a 50 Ω terminator (Mini-Circuits, BTRM-50 +) and filtered with a 9.5–11.5 MHz bandpass filter (Mini-Circuits, BBP-10.7+) to reduce the laser noise. Stimulated Raman loss signal in the pump beam was demodulated at 10 MHz using a lock-in amplifier (Stanford Research Systems, SR844 or Zurich instrument, HF2LI). The in-phase signal was sent to the microscope analog interface box (Olympus, FV30-ANALOG) to generate SRS image.

All SRS images were acquired with a 30 µs time constant set by the lock-in amplifier and 40 or 80 µs pixel dwell time. SRS spectra were measured by scanning pump laser wavelength from 870 to 892 nm, corresponding to wavenumbers from 1520 to 1800 cm^{-1}. The scanning step size of pump laser was 0.5 nm. Hyperspectral SRS imaging of secondary structure was measured with pump laser at 882.8, 881.3, 880.1, 878.8, and 875.6 nm for in vitro samples. In cells or tissues, hyperspectral secondary structure imaging was performed with pump laser at 882.8, 881.3, 880.1, 878.8, and 877.6 nm. Typical laser powers measured after the objective were 80–90 mW for the pump beam and 70–120 mW for the Stokes beam.

Bright-field and fluorescence images were acquired by the same confocal laser microscope (Olympus, FV3000) with CW laser excitation (405, 488, 561, and 640 nm) and standard bandpass filter sets. All images were analyzed and assigned color by ImageJ. All color bar values were shown in arbitrary units unless otherwise specified.

Hyperspectral SRS measurement of proteins

BSA (Bide, BD118650), OVA (Bide, BD01372421), hen egg-white lysozyme (Bide, BD01380384), human serum albumin (HSA, Sigma-Aldrich, SLCD9951), trypsin (Meryer, M29011), β-lactoglobulin (Psaitong, L10254), papain (Sigma-Aldrich, SLCN2335), and phosvitin (Rhawn, RH488977) were measured at 100–200 mg/mL in phosphate-buffered saline (PBS, pH 7.4). EGFP was measured at 50 mg/mL in urea buffer (pH 5.0, 20 mM Tris-HCl, 1 M urea). Lysozyme fibril was obtained by incubating lysozyme solution (17 mg/mL, 175 mM NaCl, pH 2.0) at 65 °C for 7 days. Concanavalin A (ConA, Sigma-Aldrich, SLCD7317) was measured at 50 mg/mL in 1 M NaCl solution. AcA(EAAAK)$_3$ANH$_2$ peptide (synthesized by GenScript China Inc., 95% purity) was measured at 15 mg/mL in water with 25% trifluoroethanol (TFE, Macklin, T819391). FUS and ATXN2 LCDs in guanidine buffer

(20 mM Tris-HCl, pH 7.4, 200 mM NaCl, 6 M guanidine-HCl) were measured at 100–200 mg/mL. All samples were measured in a chamber with a glass slide and a 0.17 mm coverslip assembled by an imaging spacer (iSpacer, IS216), unless otherwise specified.

Spontaneous Raman spectroscopy

Spontaneous Raman spectra were acquired using an upright confocal Raman microscope (HORIBA, LabRAM HR Evolution) with LabSpec6 software. A 532 nm laser with ~50 mW power was used to excite the sample through a 50× air objective (Olympus, LMPlanFLN, 0.5 N.A.). The spectral resolution is ≤0.65 cm^{-1}. BSA, deoxythymidine (Meryer, M18058), deoxyuridine (Meryer, I50004), deoxyguanosine (Meryer, I50083), and oleic acid (Energy chemical, A012216) were measured with 80 s acquisition time.

Circular dichroism (CD) spectroscopy

Circular dichroism spectra were acquired using a CD spectrometer (Applied Photophysics, Chirascan plus). Measurements were taken at room temperature from 190 to 260 nm with 1 nm bandwidth and 0.5 s per point, and averaged for three times. $AcA(EAAAK)_3ANH_2$ peptide was measured at 0.15 mg/mL in water with 25% trifluoroethanol. Concanavalin A was measured at 0.15 mg/mL in water. Phosvitin was measured at 0.15 mg/mL in 20 mM phosphate buffer (pH 7.4). The secondary structure was analyzed with the CDNN software after subtracting the solvent background.

Plasmid construction and cloning

The coding sequences of FUS LCD (residues 1-214) and ATXN2 LCD (residues 1125-1312) were amplified from human cDNA and cloned into the pHis-parallel vector with an N-terminal 6×His tag. All ATXN2 LCD and FUS LCD mutations were introduced by site-directed mutagenesis. The plasmids were transformed into DH5α *Escherichia coli* cells and cloned by HiPure Plasmid EF Mini Kit (Magen, P1112-02).

The EGFP-Htt-Q74 plasmid was purchased from Addgene (#40262). The Htt-Q74 plasmid was obtained by deleting EGFP sequence from the EGFP-Htt-Q74 plasmid. The subcloning was done by GenScript China Inc. The plasmids were transformed into Stbl2 *E. coli* cells and cloned by HiPure Plasmid EF Mini Kit.

Protein expression and purification

Recombinant proteins were expressed using BL21-(DE3)-RIPL *E. coli* cells. BL21(DE3) cells were transformed with corresponding plasmids and plated on LB agar with ampicillin selection for overnight at 37 °C. Single colonies were selected and inoculated into a 5 mL LB culture, which was allowed to grow overnight at 37 °C in a shaker at 220 rpm. The culture was added into 1 L of LB media and grown at 37 °C until the OD_{600} reached 0.6 before induction of protein expression. Cells were induced with 0.5 mM IPTG at 37 °C for 4 h at 220 rpm, followed by harvesting through centrifugation at 3470 *g* for 25 min at 4 °C. The pellet was resuspended in denaturing lysis buffer (20 mM Tris-HCl, pH 7.4, 200 mM NaCl, 6 M guanidine-HCl, 0.1 mM PMSF, 20 mM β-mercaptoethanol) with protease inhibitor cocktail (Sigma-Aldrich 539134), and sonicated for 20 min (10 s on / 10 s off, 180 W) with a cell ultrasonic crusher. After centrifugation at 20,000 *g* for 40 min, the supernatant was collected and loaded onto Ni-NTA Resin (GenScript) for 30 min at 4 °C. The Ni-NTA Resin was washed with wash buffer (20 mM Tris-HCl, pH 7.4, 200 mM NaCl, 6 M guanidine-HCl, 0.1 mM PMSF, 20 mM β-mercaptoethanol, and 25 mM imidazole) and eluted with elution buffer (200 mM NaCl, 20 mM Tris-HCl, pH 7.4, 6 M guanidine-HCl, 0.1 mM PMSF, 20 mM β-mercaptoethanol, and 300 mM imidazole). The purified proteins were concentrated to 3–6 mM using an Amicon filter (Millipore, UFC9010) and stored at −80 °C. The purity of all proteins was confirmed by SDS-PAGE.

In vitro phase separation assays of FUS and ATXN2 LCDs

Phase-separated protein condensates were prepared by rapid dilution of 4 mM stock solution to 160 μM in neutral Tris-HCl buffer (pH 7.4, 20 mM Tris-HCl, 200 mM NaCl) for both FUS and ATXN2 proteins, unless otherwise specified. Phase-separated solution was immediately added into the assembled chamber for subsequent imaging.

Aging of FUS LCD condensates was performed by dilution of stock solution to 100 μM in neutral Tris-HCl buffer added with 2% glycerol (Zancheng, CD12G201) and 10% dextran 70 (Bide, BD01376336). Phase-separated solution was added into the chamber and incubated for specified time at 37 °C before imaging. For thioflavin T staining, phase-separated solution was incubated with 50 μM ThT (Meryer, M64470), and fluorescence imaging was performed with 488 nm excitation and 500–600 nm detection.

FRAP measurements

FUS and ATXN2 LCDs were labeled with 200 ng/mL Alexa Fluor 488-C5-maleimide (Thermo Fisher Scientific, A10254) by incubating in the dark for 1 h on ice. Spin desalting columns (Cytiva, 28918006PD) were used to remove free dyes. In FRAP, fluorescent labeled protein condensates were photobleached with a 488 nm laser pulse, and the recovery of fluorescence intensity was monitored for 250 s at 5 s interval. Fluorescence signal was measured at 488 nm excitation and 500–600 nm detection.

Cell culture

U-2 OS cells (HTB-96, ATCC) were cultured in the DMEM medium (HyClone, SH30022.01), supplemented with 10% fetal bovine serum (Gemini, 900–108) and 1% penicillin-streptomycin (HyClone, SV30010) at 37 °C and 5% CO_2. Cells were seeded on 14 mm diameter round glass coverslips (NEST, 801010) with 60,000–100,000 cells per well. All cell samples were washed with DPBS (with Ca^{2+} and Mg^{2+}, HyClone, SH30264.01) for two times and assembled into a chamber filled with DPBS before imaging unless otherwise specified.

Hyperspectral SRS and fluorescence imaging of Htt proteins in live cells

U-2 OS cells were cultured for 24 h to reach 70%–80% confluence, and 500 ng EGFP-Htt-Q74 or Htt-Q74 plasmids were transfected with 1.0 μL Lipofectamine 3000 (Invitrogen, L3000) per well. After 12 h of transfection, cell medium was changed to pre-warmed regular DMEM, and incubated for another 36 h. Cell samples were washed twice with DPBS before imaging.

For immuno-imaging of unlabeled Htt-Q74, transfected cells cultured in glass-bottom dish (NEST, 801002) were first imaged by SRS, then washed once with DPBS and fixed in 4.0% PFA for 15 min at room temperature. After blocking with 3% BSA and 0.1% Triton X-100 (Yuanye, R21411) in DPBS (PBST) for 30 min at room temperature, cells were incubated with primary antibody against the Nt17 domain of Htt (Abcam, ab109115) at a dilution of 1/500 in PBST for 12 h at 4 °C. Cells were then washed five times with PBST and incubated for 1 h at room temperature in darkness with secondary antibody goat anti-rabbit Alexa647 (Abcam, ab150079) at a dilution of 1/800 in PBST. Cell samples were washed five times with PBST and twice with DPBS before fluorescence imaging of the same regions as in SRS.

For imaging of cells with triton treatment, cells cultured in glass-bottom dish were first imaged by SRS and then fixed in 4.0% PFA for 15 min at room temperature. After washing with DPBS for three times, cells were treated with 0.3% Triton X-100 for 20 min at room temperature to remove lipids and washed five times with DPBS before SRS imaging of the same field of view.

Hyperspectral SRS imaging of mouse liver tissues

All animal experiments were conducted following the guidelines and approval of the Institutional Animal Care & Use Committee and the Animal Welfare and Ethics Committee of Tsinghua University. Housing conditions included pathogen-free barrier facilities, with a 12-h light/12-h dark cycle, a maximum of five animals per cage, and ambient temperatures maintained at 22–26 °C. Mice had ad libitum access to sterile pellet food and water.

C57BL/6J mice, aged 2 years, were deeply anesthetized (Avertin, i.p.) and subsequently perfused intracardially with ice-cold 0.01 M PBS, followed by 4% PFA in PBS. After perfusion, liver tissues were dissected and post-fixed overnight at 4 °C in 4% PFA. Subsequently, tissues were rinsed in PBS and immersed in 30% sucrose in PBS for 24 h, followed by embedding in optimal cutting temperature compound and freezing on dry ice. Coronal sections of liver (7 μm) were cut with a cryostat (Leica, CM3050S) at −20 °C. Prior to immunostaining, tissue sections were permeabilized with 0.5% Triton X-100 in PBS for 30 min at room temperature and blocked with 10% normal goat serum for 1 h. The tissues were stained with primary antibody against ATXN2L (Proteintech, 24822-1-AP) overnight at 4 °C, and followed by secondary antibody goat anti-rabbit Alexa594 (Thermo Fisher Scientific, A-11012) at room temperature in darkness for 1 h.

Data processing and statistical analysis

Spectral fitting of SRS spectrum was performed using OriginPro 2017 with parameters shown in Supplementary Table 1, and Levenberg–Marquardt algorithm without weighting was applied. Linear unmixing of hyperspectral SRS images was performed as described in Supplementary Note 1 using custom code in MATLAB R2022a. FRAP data were analyzed with OriginPro 2017. All plots and statistical tests were performed using GraphPad Prism 9.5.0. The unpaired *t*-test was used for comparing two groups unless otherwise specified. No adjustments were made for multiple comparisons in all figures.

Reporting summary

Further information on research design is available in the Nature Portfolio Reporting Summary linked to this article.

Data availability

Unless otherwise stated, all data supporting the results of this study can be found in the article, supplementary, and source data files. Source data are provided with this paper.

Code availability

The custom code used in this study is available in the Supplementary Information and has been deposited in Zenodo https://doi.org/10.5281/zenodo.16811151[68].

References

1. Taylor, J. P., Hardy, J. & Fischbeck, K. H. Toxic proteins in neurodegenerative disease. *Science* **296**, 1991–1995 (2002).
2. Shin, Y. & Brangwynne, C. P. Liquid phase condensation in cell physiology and disease. *Science* **357**, eaaf4382 (2017).
3. Gao, Y. F., Li, X., Li, P. L. & Lin, Y. A brief guideline for studies of phase-separated biomolecular condensates. *Nat. Chem. Biol.* **18**, 1307–1318 (2022).
4. Kato, M. et al. Cell-free formation of RNA granules: low complexity sequence domains form dynamic fibers within hydrogels. *Cell* **149**, 753–767 (2012).
5. Molliex, A. et al. Phase separation by low complexity domains promotes stress granule assembly and drives pathological fibrillization. *Cell* **163**, 123–133 (2015).
6. Wang, J. et al. A molecular grammar governing the driving forces for phase separation of prion-like RNA binding proteins. *Cell* **174**, 688–699 (2018).
7. Alberti, S. & Dormann, D. Liquid-liquid phase separation in disease. *Annu. Rev. Genet.* **53**, 171–194 (2019).
8. Luo, F. et al. Atomic structures of FUS LC domain segments reveal bases for reversible amyloid fibril formation. *Nat. Struct. Mol. Biol.* **25**, 341–346 (2018).
9. Lee, M., Ghosh, U., Thurber, K. R., Kato, M. & Tycko, R. Molecular structure and interactions within amyloid-like fibrils formed by a low-complexity protein sequence from FUS. *Nat. Commun.* **11**, 5735 (2020).
10. Murray, D. T. et al. Structure of FUS protein fibrils and its relevance to self-assembly and phase separation of low-complexity domains. *Cell* **171**, 615–627 (2017).
11. Murthy, A. C. et al. Molecular interactions underlying liquid-liquid phase separation of the FUS low-complexity domain. *Nat. Struct. Mol. Biol.* **26**, 637–648 (2019).
12. Ganim, Z. et al. Amide I two-dimensional infrared spectroscopy of proteins. *Acc. Chem. Res.* **41**, 432–441 (2008).
13. Ghosh, A., Ostrander, J. S. & Zanni, M. T. Watching proteins wiggle: mapping structures with two dimensional infrared spectroscopy. *Chem. Rev.* **117**, 10726–10759 (2017).
14. Edun, D. N., Flanagan, M. R. & Serrano, A. L. Does liquid-liquid phase separation drive peptide folding?. *Chem. Sci.* **12**, 2474–2479 (2021).
15. Rygula, A. et al. Raman spectroscopy of proteins: a review. *J. Raman Spectrosc.* **44**, 1061–1076 (2013).
16. Devitt, G., Howard, K., Mudher, A. & Mahajan, S. Raman spectroscopy: an emerging tool in neurodegenerative disease research and diagnosis. *ACS Chem. Neurosci.* **9**, 404–420 (2018).
17. Baiz, C. R., Peng, C. S., Reppert, M. E., Jones, K. C. & Tokmakoff, A. Coherent two-dimensional infrared spectroscopy: quantitative analysis of protein secondary structure in solution. *Analyst* **137**, 1793–1799 (2012).
18. Minnes, L. et al. Quantifying secondary structure changes in calmodulin using 2D-IR spectroscopy. *Anal. Chem.* **89**, 10898–10906 (2017).
19. Weeks, W. B. & Buchanan, L. E. Label-free detection of β-sheet polymorphism. *J. Phys. Chem. Lett.* **13**, 9534–9538 (2022).
20. Lorenz-Ochoa, K. A., Cho, M., Parekh, S. H. & Baiz, C. R. Interaction-dependent secondary structure of peptides in biomolecular condensates. *J. Am. Chem. Soc.* **146**, 33616–33625 (2024).
21. Maiti, N. C., Apetri, M. M., Zagorski, M. G., Carey, P. R. & Anderson, V. E. Raman spectroscopic characterization of secondary structure in natively unfolded proteins: α-synuclein. *J. Am. Chem. Soc.* **126**, 2399–2408 (2004).
22. Shuster, S. O. & Lee, J. C. Watching liquid droplets of TDP-43(CTD) age by Raman spectroscopy. *J. Biol. Chem.* **298**, 101528 (2022).
23. Wang, Q. J. et al. Protein secondary structure in spider silk nanofibrils. *Nat. Commun.* **13**, 4329 (2022).
24. Dolui, S. et al. Raman spectroscopic insights of phase-separated insulin aggregates. *ACS Phys. Chem. Au* **4**, 268–280 (2024).
25. Avni, A., Joshi, A., Walimbe, A., Pattanashetty, S. G. & Mukhopadhyay, S. Single-droplet surface-enhanced Raman scattering decodes the molecular determinants of liquid-liquid phase separation. *Nat. Commun.* **13**, 4378 (2022).
26. Freudiger, C. W. et al. Label-free biomedical imaging with high sensitivity by stimulated Raman scattering microscopy. *Science* **322**, 1857–1861 (2008).
27. Min, W., Freudiger, C. W., Lu, S. J. & Xie, X. S. Coherent nonlinear optical imaging: beyond fluorescence microscopy. *Annu. Rev. Phys. Chem.* **62**, 507–530 (2011).
28. Cheng, J. X. & Xie, X. S. Vibrational spectroscopic imaging of living systems: an emerging platform for biology and medicine. *Science* **350**, aaa8870 (2015).
29. Camp, C. H. & Cicerone, M. T. Chemically sensitive bioimaging with coherent Raman scattering. *Nat. Photonics* **9**, 295–305 (2015).

30. Hu, F. H., Shi, L. X. & Min, W. Biological imaging of chemical bonds by stimulated Raman scattering microscopy. *Nat. Methods* **16**, 830–842 (2019).
31. Fu, D. et al. Metabolic fingerprinting of neutral lipids with hyperspectral stimulated Raman scattering microscopy. *J. Am. Chem. Soc.* **136**, 8820–8828 (2014).
32. Lu, F. K. et al. Label-free DNA imaging in vivo with stimulated Raman scattering microscopy. *Proc. Natl. Acad. Sci.* **112**, 11624–11629 (2015).
33. Ji, M. B. et al. Label-free imaging of amyloid plaques in Alzheimer's disease with stimulated Raman scattering microscopy. *Sci. Adv.* **4**, eaat7715 (2018).
34. Oh, S. et al. Protein and lipid mass concentration measurement in tissues by stimulated Raman scattering microscopy. *Proc. Natl. Acad. Sci.* **119**, e2117938119 (2022).
35. Ma, Y. et al. Nucleobase clustering contributes to the formation and hollowing of repeat-expansion RNA condensate. *J. Am. Chem. Soc.* **144**, 4716–4720 (2022).
36. Zhang, W. X. et al. Multi-molecular hyperspectral PRM-SRS microscopy. *Nat. Commun.* **15**, 1599 (2024).
37. Chatterjee, S. et al. Reversible kinetic trapping of FUS biomolecular condensates. *Adv. Sci.* **9**, 2104247 (2022).
38. Bagchi, B. Water dynamics in the hydration layer around proteins and micelles. *Chem. Rev.* **105**, 3197–3219 (2005).
39. Yokosawa, K. et al. Concentration quantification of the low-complexity domain of fused in sarcoma inside a single droplet and effects of solution parameters. *J. Phys. Chem. Lett.* **13**, 5692–5697 (2022).
40. Zheng, W. W. et al. Molecular details of protein condensates probed by microsecond long atomistic simulations. *J. Phys. Chem. B* **124**, 11671–11679 (2020).
41. Watson, J. L. et al. Macromolecular condensation buffers intracellular water potential. *Nature* **623**, 842–852 (2023).
42. Joshi, A. et al. Hydrogen-bonded network of water in phase-separated biomolecular condensates. *J. Phys. Chem. Lett.* **15**, 7724–7734 (2024).
43. Pezzotti, S., König, B., Ramos, S., Schwaab, G. & Havenith, M. Liquid-liquid phase separation? ask the water!. *J. Phys. Chem. Lett.* **14**, 1556–1563 (2023).
44. Lorenz-Ochoa, K. A. & Baiz, C. R. Ultrafast spectroscopy reveals slow water dynamics in biocondensates. *J. Am. Chem. Soc.* **145**, 27800–27809 (2023).
45. Ahlers, J. et al. The key role of solvent in condensation: mapping water in liquid-liquid phase-separated FUS. *Biophys. J.* **120**, 1266–1275 (2021).
46. Mukherjee, S. & Schäfer, L. V. Thermodynamic forces from protein and water govern condensate formation of an intrinsically disordered protein domain. *Nat. Commun.* **14**, 5892 (2023).
47. Zhang, Y. M., Li, S. L., Gong, X. P. & Chen, J. H. Toward accurate simulation of coupling between protein secondary structure and phase separation. *J. Am. Chem. Soc.* **146**, 342–357 (2023).
48. Patel, A. et al. A liquid-to-solid phase transition of the ALS protein FUS accelerated by disease mutation. *Cell* **162**, 1066–1077 (2015).
49. Ray, S. et al. -Synuclein aggregation nucleates through liquid-liquid phase separation. *Nat. Chem.* **12**, 705–716 (2020).
50. Garaizar, A. et al. Aging can transform single-component protein condensates into multiphase architectures. *P. Natl. Acad. Sci.* **119**, e2119800119 (2022).
51. Michaels, T. C. T. et al. Amyloid formation as a protein phase transition. *Nat. Rev. Phys.* **5**, 379–397 (2023).
52. Yang, Y. S. et al. Yeast Ataxin-2 forms an intracellular condensate required for the inhibition of TORC1 signaling during respiratory growth. *Cell* **177**, 697–710 (2019).
53. Zhou, X. M. et al. Mutations linked to neurological disease enhance self-association of low-complexity protein sequences. *Science* **377**, eabn5582 (2022).
54. Saudou, F. & Humbert, S. The biology of huntingtin. *Neuron* **89**, 910–926 (2016).
55. Riguet, N. et al. Nuclear and cytoplasmic huntingtin inclusions exhibit distinct biochemical composition, interactome and ultrastructural properties. *Nat. Commun.* **12**, 6579 (2021).
56. Miao, K. & Wei, L. Live-cell imaging and quantification of PolyQ aggregates by stimulated Raman scattering of selective deuterium labeling. *ACS Cent. Sci.* **6**, 478–486 (2020).
57. Sivanandam, V. N. et al. The aggregation-enhancing huntingtin N-terminus is helical in amyloid fibrils. *J. Am. Chem. Soc.* **133**, 4558–4566 (2011).
58. Chen, M. C. & Wolynes, P. G. Aggregation landscapes of Huntingtin exon 1 protein fragments and the critical repeat length for the onset of Huntington's disease. *P. Natl. Acad. Sci.* **114**, 4406–4411 (2017).
59. Chen, Y. R. et al. Tissue-specific landscape of protein aggregation and quality control in an aging vertebrate. *Dev. Cell* **59**, 1892–1911 (2024).
60. Kaehler, C. et al. Ataxin-2-like is a regulator of stress granules and processing bodies. *PLoS ONE***7**, e50134 (2012).
61. Qamar, S. et al. FUS phase separation is modulated by a molecular chaperone and methylation of arginine cation-π interactions. *Cell* **173**, 720–734 (2018).
62. Shen, Y. et al. The liquid-to-solid transition of FUS is promoted by the condensate surface. *P. Natl. Acad. Sci.* **120**, e2301366120 (2023).
63. He, C. D., Wu, C. Y., Li, W. & Xu, K. Multidimensional super-resolution microscopy unveils nanoscale surface aggregates in the aging of FUS condensates. *J. Am. Chem. Soc.* **145**, 24240–24248 (2023).
64. Emmanouilidis, L. et al. A solid beta-sheet structure is formed at the surface of FUS droplets during aging. *Nat. Chem. Biol.* **20**, 406–407 (2024).
65. Murthy, A. C. & Fawzi, N. L. The (un)structural biology of biomolecular liquid-liquid phase separation using NMR spectroscopy. *J. Biol. Chem.* **295**, 2375–2384 (2020).
66. Jang, H. et al. Super-resolution SRS microscopy with A-PoD. *Nat. Methods* **20**, 448–458 (2023).
67. Gilbert, M. A. G. et al. CryoET of beta-amyloid and tau within post-mortem Alzheimer's disease brain. *Nature* **631**, 913–919 (2024).
68. Sun, R. F. & Hu, F. H. Image unmixing code of protein secondary structure by hyperspectral stimulated Raman scattering microscopy. Zenodo. https://doi.org/10.5281/zenodo.16811151 (2025).

Acknowledgements

This work was supported by the National Key Research and Development Program of China (2021YFA1200103 to F.H.), the National Natural Science Foundation of China (22174085 to F.H. and 32350027 to Y.L.), the Ministry of Science and Technology of the People's Republic of China (2022ZD0204900 to Y.L.), and Tsinghua University Initiative Scientific Research Program.

Author contributions

F.H. conceived the research. R.S., Y.Z., Y.L., and F.H. designed the experiments. R.S. completed all imaging studies and analyzed the data. Y.Z. carried out protein and tissue sample preparation. Y.L. and F.H. supervised the project. R.S. and F.H. wrote the manuscript with inputs from all authors.

Competing interests

The authors declare no competing interests.

Additional information

Supplementary information The online version contains supplementary material available at https://doi.org/10.1038/s41467-025-63894-1.

Correspondence and requests for materials should be addressed to Yi Lin or Fanghao Hu.

Peer review information *Nature Communications* thanks Dan Fu and the other anonymous reviewer(s) for their contribution to the peer review of this work. A peer review file is available.